RSC Advances

PAPER

View Article Online
View Journal | View Issue

Cite this: *RSC Adv.*, 2021, **11**, 37254

Highly efficient visible light active Cu–ZnO/S-g-C_3N_4 nanocomposites for efficient photocatalytic degradation of organic pollutants†

Mohsin Javed,*[a] Muhammad Azam Qamar, *[a] Sammia Shahid,[a] Hashem O. Alsaab[b] and Salma Asif[a]

Received 27th September 2021
Accepted 29th October 2021

DOI: 10.1039/d1ra07203j

rsc.li/rsc-advances

The photocatalytic activity of photocatalysts is severely hampered by limited visible light harvesting and unwanted fast recombination of photogenerated e^- and h^+. In the current study, the photocatalytic efficiency of Cu–ZnO/S-g-C_3N_4 (CZS) nanocomposites was investigated against MB dye. The composite materials were designed *via* chemical co-precipitation method and characterised by important analytical techniques. Distinctive heterojunctions developed between S-g-C_3N_4 and Cu–ZnO in the CZS composite were revealed by TEM. The synthesized composites exhibit a huge number of active sites, a large surface area, a smaller size and better visible light absorption. The considerable enhancement in the photocatalytic activity of CZS nanocomposites might be accredited to the decay in the e–h pair recombination rate and a red shift in the visible region, as observed by PL and optical analysis, respectively. Furthermore, the metal (Cu) doping into the S-g-C_3N_4/ZnO matrix created exemplary interfaces between ZnO and S-g-C_3N_4, and maximized the photocatalytic activity of CZS nanocomposites. In particular, CZS nanocomposites synthesized by integrating 25% S-g-C_3N_4 with 4% Cu–ZnO (CZS-25 NCs) exhibited the 100% photocatalytic degradation of MB in 60 minutes under sunlight irradiation. After six cycles, the photocatalytic stability of CZS-25 NCs was excellent. Likewise, a plausible MB degradation mechanism is proposed over CZS-25 NCs based on photoluminescence and reactive species scavenger test observation. The current research supports the design of novel composites for the photocatalytic disintegration of organic contaminants.

1. Introduction

Waste industrialization and subsequent pollution are certainly among the significant problems the world faces presently. Human activities have evolved different substances such as metal ions, organic pollutants, and pesticides, becoming a major threat for living beings. These organic pollutants need to be degraded to lower their impact on the environment because they tend to be toxic.[1–3] Primarily, water pollution demands focus urgently. Semiconductor photocatalysis can be an excellent solution to the severe problem of pollution.[4–7] To date, numerous metal oxides, such as ZnO, WO_3, In_2O_3, SnO_2, Cu_2O and TiO_2, have been used for the photocatalytic degradation of contaminants.[8–10] Because of its low cost, outstanding stability, high yield, and good optical properties, ZnO is a potential photocatalyst.[11,12] Unfortunately, the light absorption of ZnO is mainly limited to the UV region, and it has almost no visible light response due to its large bandgap (~3.37 eV).[13,14] Moreover, ZnO has some issues, such as low charge separation and photocorrosion. These problems have hindered the practical applications of ZnO in photocatalysis.[15] Different techniques, including doping with ions and composite formation with semiconductors, were employed to overcome the inherent deficiencies of ZnO.[16,17] Metal ion-doped ZnO has improved visible light absorption and photocatalytic activity.[18–20] Various transition elements, such as Ni, Fe, Cr, Mn, and Cu, have been used to elevate the photocatalytic efficiency of ZnO.[21] Cu is thought to be the most effective metal ion dopant for improving the photocatalytic competence of ZnO. Cu-doping produces defects in the ZnO lattice, and improves the optical and electrical properties. The Cu-doped ZnO with corn seed morphology exhibited 3.5 times better methyl orange photocatalytic degradation than pure ZnO.[22] Vaiano *et al.* reported the complete oxidation of As(III) to As(V) within 120 minutes by Cu-doped ZnO nanoparticles under sunlight.[23] The photocatalytic efficiency of Cu–ZnO/TiO_2 was assessed against MO dye under sunlight, and 3% Cu–ZnO/TiO_2 NPs exhibited approximately 28.3 and 12 times better catalytic efficiency than TiO_2 and ZnO/TiO_2,

---

[a] *Department of Chemistry, School of Science, University of Management and Technology, Lahore 54770, Pakistan. E-mail: mohsin.javed@umt.edu.pk; qamariub@gmail.com*

[b] *Department of Pharmaceutics and Pharmaceutical Technology, Taif University, P. O. Box 11099, Taif 21944, Saudi Arabia*

† Electronic supplementary information (ESI) available. See DOI: 10.1039/d1ra07203j

respectively.[24] Researchers found that oxygen vacancies and carbonaceous species increased the photocatalytic activity of ZnO. Oxygen vacancies can reduce the bandgap energy of ZnO by forming shallow levels of oxygen vacancies that partially overlapped the ZnO valence band. Furthermore, the creation of additional levels below the conduction band (CB) of ZnO can narrow the band gap.[25] Carbon species, including multi-wall carbon nanotube, g-C_3N_4 and graphenes, when incorporated with ZnO, acted as both photo-sensitizers and stabilisers.

It is widely known that modifying ZnO with a suitable semiconductor, such as g-C_3N_4, can effectively inhibit the electron–hole recombination and improve the photocatalytic activity. g-C_3N_4, as a polymeric semiconductor, has remarkable stability, good mechanical, thermal, optical, and electrical properties, and cost-effectiveness.[26] It has proper absorption in the visible region (up to 450 nm), and an appropriate bandgap (~2.7 eV) that makes it a potential photocatalyst for water splitting and pollution degradation.[27] Conversely, the pristine g-C_3N_4 has some intrinsic limitations, such as relatively lower quantum efficiency and inadequate visible light absorption.[28] As a result, the photocatalytic effectiveness of g-C_3N_4 in its pure form is insufficient for practical use. To boost the photocatalytic activity, the bandgap of g-C_3N_4 can be lowered by doping with sulfur. The S-doping modifies the bandgap of g-C_3N_4 by stacking its 2p orbitals on the VB of bulk g-C_3N_4, and improves the e–h pairs' mobility and separation. Hong *et al.* detailed that a better photocatalytic H_2 (30 times) was produced by mesoporous S-g-C_3N_4 than pristine g-C_3N_4.[29] Wang *et al.* stated that S-g-C_3N_4 exhibited a nearly 1.38 times better photocatalytic CO_2 reduction rate than pristine g-C_3N_4.[30] In another study, porous S-g-C_3N_4 showed improved adsorption and photocatalytic degradation of rhodamine B dye compared to pure g-C_3N_4 under visible light.[31] Theoretically and experimentally, it has been recognized that S-doping has revised the g-C_3N_4 structurally, reduced its E_g value, and improved its e–h pair separation efficiency.[32] To boost the photocatalytic activity of ZnO/g-C_3N_4, we used the concept of the coordinated action of both non-metal (sulphur) doped g-C_3N_4 and metal (Cu) doped ZnO in the nanocomposites.

So, it looks vital to combine the S-g-C_3N_4 and Cu–ZnO NPs to produce a hybrid composite (S-g-C_3N_4/Cu–ZnO) with excellent catalytic properties. In the study, a series of S-g-C_3N_4/Cu–ZnO nanocomposites (NCs) was made by physical mixing of variable amounts of S-g-C_3N_4 with Cu–ZnO NPs, and the photocatalytic efficiency of the resultant ternary composites was investigated against the MB dye. The comparative photocatalytic MB degradation by S-g-C_3N_4/Cu–ZnO NCs indicates that the heterojunction with ratio (3 : 1 = S-g-C_3N_4 : Cu–ZnO) exhibited a maximum of 97% degradation of dye in 60 minutes. Due to the hybridization of diverse materials, more and more active sites are produced, which increases the e–h pairs separation and catalytic efficiency of the composites.

2. Materials and methods

2.1 Materials

Analytical grade thiourea ($(NH_2)_2CS$, ≥99.5%), copper nitrate trihydrate ($Cu(NO_3)_2 \cdot 3H_2O$, 99%), methylene blue ($C_{16}H_{18}N_3SCl$, ≥99.0%), zinc nitrate hexahydrate ($Zn(NO_3)_2 \cdot 6H_2O$, 99%), ammonia solution (25%), ammonium oxalate ($C_2H_8N_2O_4$, ≥99.0%), ethanol (C_2H_5OH), isopropanol (C_3H_8O, ≥99.9%), and benzoquinone ($C_6H_4O_2$, 99.5%) were bought from Merck and consumed without any purification.

2.2 Synthesis of ZnO NPs

ZnO and Cu-doped ZnO nanoparticles (NPs) were prepared *via* the co-precipitation mode.[33] For the synthesis of ZnO, sodium hydroxide solution (4 M) was added dropwise into 0.04 M solution of Zn $(NO_3)_2 \cdot 6H_2O$ (2.97 g/250 ml) with constant stirring. At pH = 11, the white precipitates yielded were washed with ethanol/DI water, and then allowed to dry at room temperature. Finally, calcination of the precipitate was carried out in a muffle furnace at 450 °C for 3 h to achieve ZnO NPs (with heating rate: 5 °C min^{-1}). Similarly, Cu–ZnO NPs with various loadings of Cu (1%, 2%, 3%, 4%, and 5%) were synthesized by following the same co-precipitation method.[33] To fabricate 1% Cu–ZnO NPs, 0.029 grams of $Cu(NO_3)_2 \cdot 3H_2O$ were dissolved in 80 ml of DI water by constant stirring and heating gently. Then, the Cu precursor solution was added to 0.04 M Zn $(NO_3)_2 \cdot 6H_2O$ solution. Then, the Cu–ZnO white precipitates were obtained by adding 25% ammonia solution. The final 1% Cu–ZnO NPs were obtained by repeating the steps, as previously described for the synthesis of ZnO. In the same way, (2%, 3%, 4%, and 5%) Cu–ZnO NPs were prepared. The synthesis conditions of the Cu–ZnO NPs with compositions are tabulated in Table 1.

2.3 Synthesis of sulphur-doped g-C_3N_4 (S-g-C_3N_4)

S-g-C_3N_4 was fabricated by heating thiourea at 3 °C min^{-1} to 550 °C for 5 hours in a muffle furnace (direct low-temperature

Table 1 Contents and synthesis conditions of Cu–ZnO NPs

		wt% ratio		
S. no.	Nanoparticles	$Cu(NO_3)_2 \cdot 3H_2O$	$Zn(NO_3)_2 \cdot 6H_2O$	MB dye degradation (%) (after 105 min)
1	ZnO	0	100	53
2	1% Cu–ZnO	1	99	55
3	2% Cu–ZnO	2	98	63
4	3% Cu–ZnO	3	97	76
5	4% Cu–ZnO	4	96	82
6	5% Cu–ZnO	5	95	61

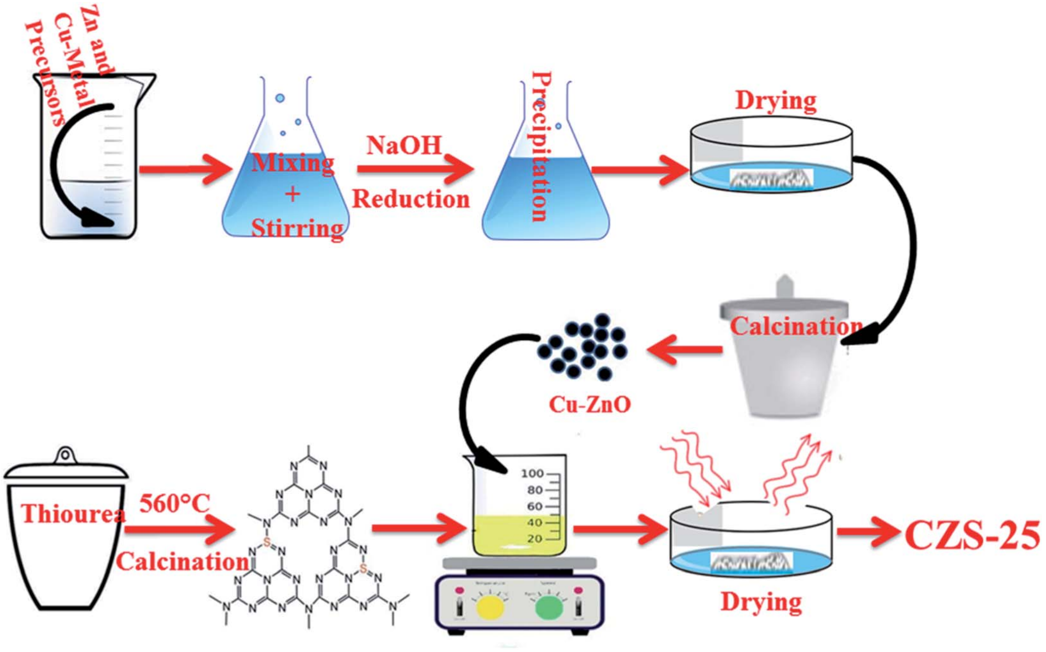

Fig. 1 Diagrammatic illustration of the synthesis of 4% Cu–ZnO/S-g-C_3N_4 composites.

thermal condensation).[34] The S-g-C_3N_4 so-attained was in the form of a yellowish porous product (Fig. 1).

2.4 Synthesis of S-g-C_3N_4/Cu–ZnO nanocomposites

The maximum MB photodegradation was exhibited by the 4% Cu–ZnO NPs in the photocatalytic degradation experiment of MB by (0, 1, 2, 3, 4 & 5%) Cu–ZnO NPs. Then, the 4% Cu–ZnO NPs were mixed with diverse amounts of S-g-C_3N_4 to yield ternary nanocomposites (NCs). Then, the ternary composite with a (1 : 1) ratio was prepared by mixing and stirring 0.1 g of 4% Cu–ZnO NPs and 0.1 g of S-g-C_3N_4 in 50 ml of ethanol. The final (1 : 1) composite was obtained by evaporating ethanol in sunlight. By following the same process, the 4% Cu–ZnO/S-g-C_3N_4 composites in (1 : 3), (1 : 5), and (3 : 1) ratios were prepared. Similarly, the ZnO/S-g-C_3N_4 composite was synthesized for comparative photocatalytic study. The detailed composition and the resultant catalytic efficiency of the 4% Cu–ZnO/S-g-C_3N_4 NCs are given in Table 2.

2.5 Characterization

The XRD (Bruker AXS, D8-S4) approach was employed to identify the structure of the fabricated catalysts, and the morphology of the fabricated catalysts was detected by SEM (Hitachi, S-4800). The elemental composition was recognised with EDS. A UV-vis-NIR diffuse reflectance spectrophotometer was used to study the photocatalytic and UV-visible absorption spectra (UV-770, Jasco). Functional groups were measured using an FT-IR spectrometer (Perkin 400 FT-IR).

2.6 Photocatalytic activity

Photocatalytic study of the photocatalysts was accomplished under sunlight by observing the photocatalytic degradation of the MB dye. 0.05 g of each photocatalyst was added to 50 ml of dye solution (10 mg L^{-1}) during the MB photocatalytic degradation experiment. Prior to conducting photocatalysis, each catalyst suspension was stirred for 0.5 hours to reach adsorption equilibrium between the catalyst and dye under dark

Table 2 Composition of 4% Cu–ZnO/S-g-C_3N_4 nanocomposites and their corresponding photocatalytic activities

		wt% ratio of heterostructures			
S. no.	Nanocomposites	S-g-C_3N_4	4% Cu@ZnO	(S-g-C_3N_4 : Cu@ZnO) ratio	Sample abbreviations
1	4% Cu–ZnO/S-g-C_3N_4	50	50	(1 : 1)	CZS-50
2	4% Cu–ZnO/S-g-C_3N_4	75	25	(3 : 1)	CZS-75
3	4% Cu–ZnO/S-g-C_3N_4	83.33	16.67	(5 : 1)	CZS-83
4	4% Cu–ZnO/S-g-C_3N_4	25	75	(1 : 3)	CZS-25
5	S-g-C_3N_4	100	00	(1 : 0)	SGN
6	4% Cu–ZnO	00	100	(0 : 1)	4-CZN
7	ZnO/S-g-C_3N_4				ZS

conditions in a customized quartz reactor. Then, each sample was provided with sunlight to start the photocatalytic degradation of MB, and 5 ml aliquots were taken out after specific intervals. The dye catalysis was performed under solar radiation at ambient conditions (68–73 k lux). The taken aliquots were centrifuged (@9000 rpm) for 9 minutes to remove any suspended particles, and then scanned on an ultraviolet-visible spectrophotometer. Then, each photocatalyst's percent dye degradation ($D\%$) was estimated by using the equation below:

$$D\% = ((C_o - C)/C_o) \times 100 \tag{1}$$

where C_o and C are the initial and any time (t) concentrations of MB, respectively.

3. Results and discussions

3.1 Morphological and compositional analysis

Fig. 2a and b show the surface morphology of the synthesized ZnO and 4-CZN catalysts, as examined by the SEM technique. In the SEM image of ZnO, several nanosheets are arranged to build flower-like 3D shapes (Fig. 2a). In Fig. 2b, the stacked thin sheet morphology of the 4-CZN is exhibited. The SGN morphology consisted of typically curled two-dimensional sheets

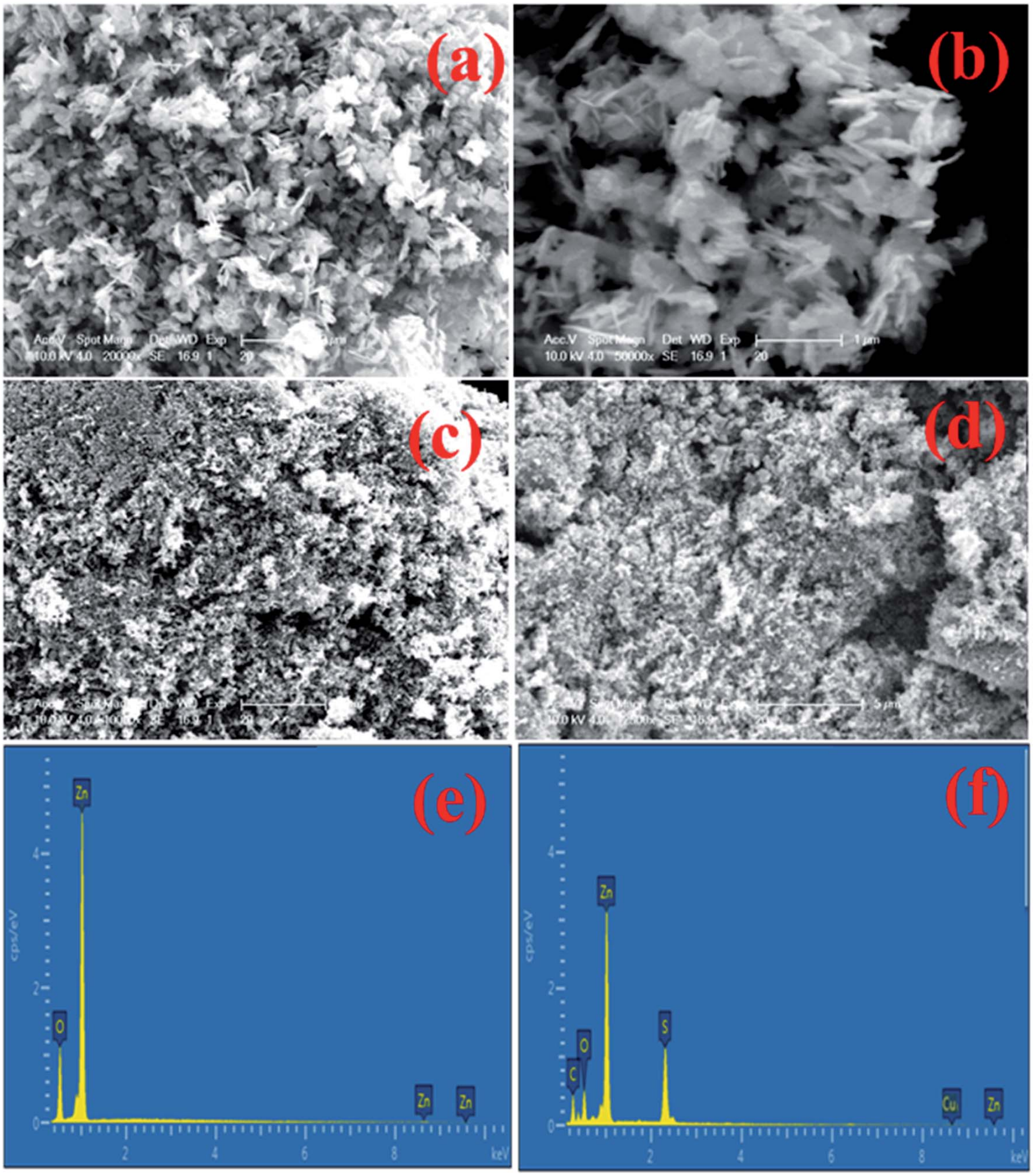

Fig. 2 (a–d) SEM morphology of the ZnO (a), 4-CZN (b), SGN (c) and CZS-25 (d) composites, and EDS spectra of ZnO (e) and CZS-25 (f) samples.

agglomerated to form bulk structures (Fig. 2c). The ternary CZS-75 photocatalyst displayed a porous, semi-round, sponge-like heterostructure with agglomeration (Fig. 2d). It is acclaimed that such heterojunction morphology increases the surface area, active sites, and corresponding photocatalytic activity of the material. Furthermore, the structural morphology of the catalysts was examined by TEM, as shown in Fig. 3a–d. The TEM images reveal the nanosized structures of ZnO and 4-CZN NPs, respectively, as shown in Fig. 3a and b. The ZnO and 4-CZN NPs show varying diameters (10–30 nm). The TEM images of ZS manifest the existing junction between the ZnO NPs and SGN sheets, as shown by Fig. 3c. The 4-CZN NPs are dispersed over the delicate sheets of SGN to design the CZS-25 heterostructure, as shown by Fig. 3d. The SGN soft sheets engross the 4-CZN NPs, which form the basis to reinforce the NPs and increase the photocatalytic efficiency of the resultant composite. The EDX analysis of the prepared materials was performed to identify their chemical elemental composition. Fig. 2e exhibits the EDX spectrum of ZnO NPs, which consists of only Zn and O elemental peaks. The EDX spectrum of the g-C_3N_4/Cu-doped ZnO composites contain C, N, S, Zn, O and Cu elemental peaks (Fig. 2f), and thus shows the purity of the synthesized composites.

3.2 XRD analysis

The purity and phase of the produced samples were investigated using XRD analysis. The XRD patterns of SGN, ZnO, 4-CZN, ZS, and CZS-25 are shown in Fig. 4a. The presence of the decisive peaks in XRD pattern of SGN at 27.4° corresponds to the crystal planes of (100) that endorse the existence of nanosheets in pristine SGN samples.[35] The characteristic diffraction peaks for ZnO appeared at 2θ values of 32.06°, 35.0°, 36.98°, 48.01°, 57.03°, 63.05°, 69.0° and at 70.04°, which stand for the crystal planes of (100), (002), (101), (102), (110), (103), (112) and (201). The observed peaks are in complete consonance with the standard XRD pattern of the hexagonal wurtzite structure of ZnO (JCPDS 00-036-1451).[36] The two-phase composition of the ZS and CZS-25 composites is endorsed by the co-existence of the characteristic diffraction peaks of 4-CZN and SGN in the corresponding XRD patterns.[37] In the XRD patterns of the CZS-25 and 4-CZN samples, a pronounced reduction in intensity and slight shifting of the major peaks ((100), (101)) towards the lower angle is noticed, which verify the effective metal (Cu) ions doping into ZnO and incorporation of 4-CZN with SGN (Fig. 4b).[38] In addition, a general broadening in the 4-CZN and

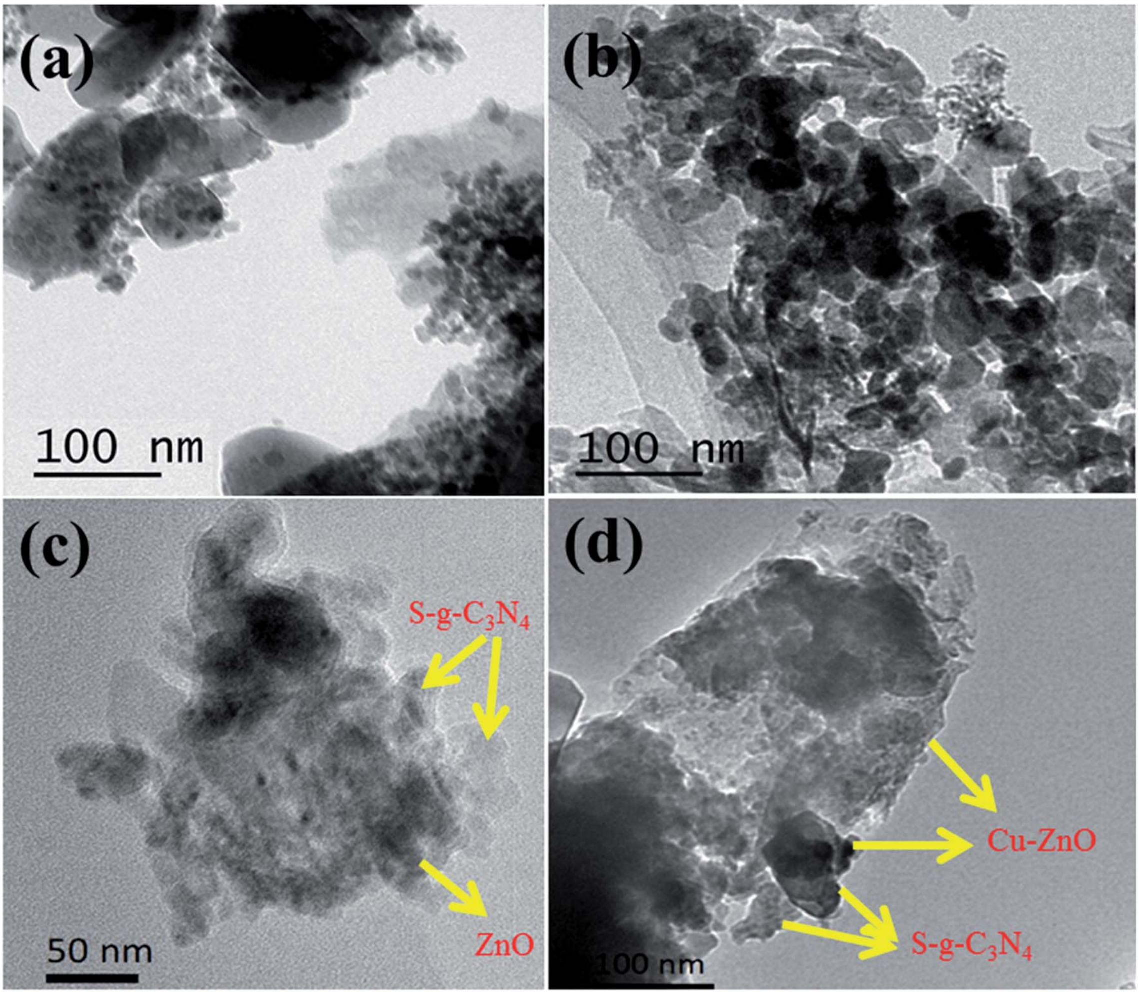

Fig. 3 TEM images of (a) ZnO, (b) 4-CZN, (c) SGN and (d) CZS-25 composites.

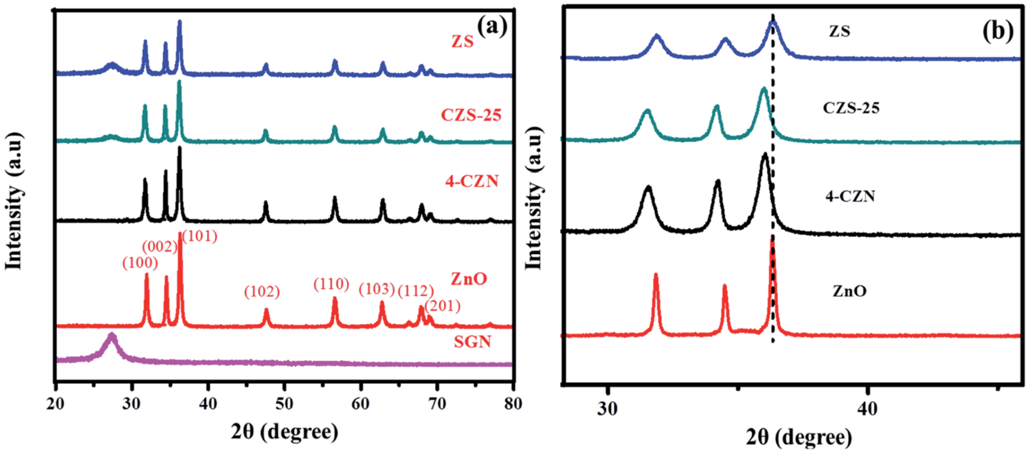

Fig. 4 (a and b) XRD pattern of ZnO, 4-CZN, ZS, SGN and CZS-25 composites.

SGN peaks and the shift towards the lower angle particular at (002) was noticeable mainly due to Cu doping.[39]

3.3 FTIR analysis

FTIR spectroscopy was used to characterize the functional groups and the chemical composition of the ZnO, 4-CZN, CZS-25, CZS-50, and CZS-75 samples (Fig. 5). The peaks occurring in ZnO NPs and 4-CZN, from 400 cm^{-1} to 500 cm^{-1}, represent the metal oxide bond (Zn–O), while the peaks from 780 cm^{-1} to 980 cm^{-1} appear due to metal peroxides (M–O–O–M).[40] A broad band at around 3350 cm^{-1} in the prepared samples is due to the stretching vibration of the –O–H bonds.[41] In the CZS-25, CZS-50, and CZS-75 composites, several strong stretching bands are detected in the 1220–1630 cm^{-1} region, which is ascribed to the heptazine repeat units of g-C_3N_4.[42] The peaks in composites at 807 cm^{-1} and about 3145 cm^{-1} are attributed to the N–H stretching frequency and the tri-*s*-triazine units, respectively.[42,43] The presence of the corresponding peaks of g-C_3N_4 and ZnO in the CZS-25, CZS-50, and CZS-75 samples validated the purity and successful formation of the composites.[44]

3.4 Optical properties

UV-visible diffuse reflectance spectroscopy was used to examine the optical properties of the produced catalysts (Fig. 6). The absorption band for pure ZnO was observed at 385 nm, indicating that ZnO NPs are unresponsive to visible radiation due to their high-energy bandgap. For 4-CZN NPs, there is a slight enhancement in visible light harvesting, which is congruent with their decreased bandgap energy (3.09 eV). In contrast to ZnO, SGN has an absorption edge at 460 nm. The absorption of the SGN exhibits an improvement because of sulfur doping into g-C_3N_4 that corresponds well with its observed bandgap energy of 2.60 eV and improved photocatalytic efficiency. Equally, the CZS-25 photocatalyst demonstrated outstanding visible-light absorption, inferring its enriched photocatalytic action under sunlight. Compared to pure ZnO and SGN, the ZS and CZS-25 NCs showed better absorption in the visible area (red-shift).

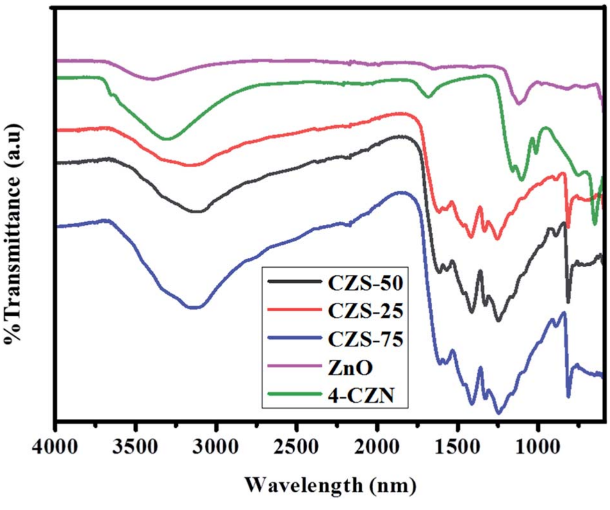

Fig. 5 FTIR analysis of the ZnO, 4-CZN, CZS-25, CZS-50 and CZS-75 composites.

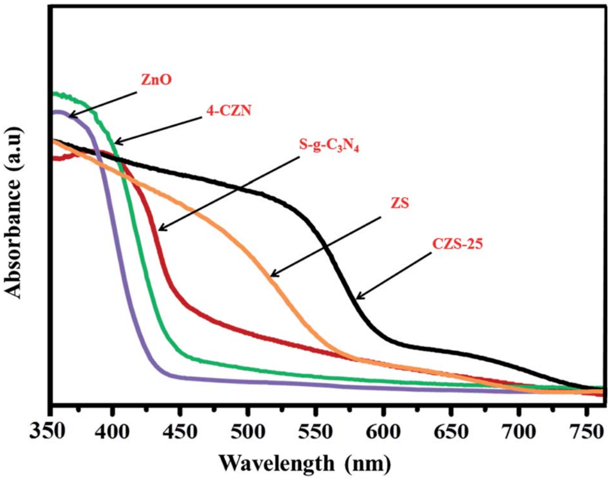

Fig. 6 UV-vis DRS absorption spectra of the ZnO, 4-CZN, ZS and CZS-25 composites.

Table 3 Energy bandgap of ZnO, 4-CZN, S-g-C_3N_4, ZS and CZS-25

S. no.	Sample	Bandgap (eV)
1	ZnO	3.22
2	4-CZN	3.09
3	S-g-C_3N_4	2.60
4	ZS	2.87
5	CZS-25	2.54

Table 3 lists the bandgap energies of the fabricated materials calculated using Tauc's relation.[45]

3.5 PL analysis

Photoluminescence (PL) spectroscopy is a common method being used to probe the charge separation capacity of the photo-excited (e–h pairs) in the photocatalytic materials.[46] The photoluminescence emission spectra of the produced catalysts observed at the excitation wavelength of 365 nm are shown in Fig. 7. The SGN has a prominent emission peak at 460 nm, indicating a high frequency of e–h pairs recombination. Compared with that of ZnO, the PL intensity of 4-CZN showed a significant drop, which can be attributed to the origin of certain trapped states and decreased density of intrinsic defects.[47] In addition, compared with the bare SGN, there is a drop in the PL peak intensity of ZS, which is attributed to the formation of a ZS heterostructure, zinc defects and surface oxygen vacancies.[48] The strong conjugation between the SGN sheets and 4-CZN NPs resulted in a low PL peak of the CZS-25 heterostructure. The interfacial transfer of charge (electrons) between ZnO and g-C_3N_4 might be responsible for the diminished PL peak and substantially decreased rate of e–h pairs recombination in the CZS-25 NCs. As cited in the previous literature, the doped transition metal assists the transfer of charge between ZnO and g-C_3N_4 in CZS NCs.[49] Thus, in the CZS-25 nanocomposites, the photo-excited electrons were effectively conducted and used up in ROS production. Thus, the degree of e–h pairs recombination in CZ-25 is repressed, and its photocatalytic activity is improved.

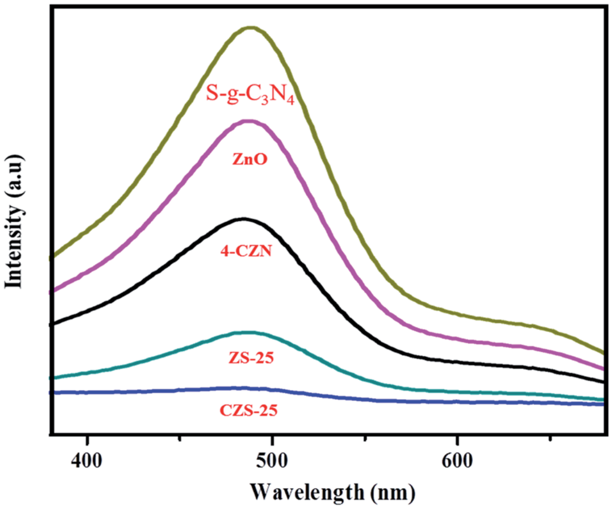

Fig. 7 PL analysis of the ZnO, 4-CZN, ZS and CZS-25 composites.

Table 4 Nitrogen physisorption data of ZnO, 4-CZN, S-g-C_3N_4, ZS-25 and CZS-25

Sample	Surface area ($m^2\ g^{-1}$)	Average pore width (Å)	Pore volume ($cm^3\ g^{-1}$)
ZnO	6.33	138.12	0.04
4-CZN	15.39	1141.22	0.06
ZS	26.24	170.10	0.09
CZS-25	63.44	84.59	0.12

3.6 Surface area analysis

The prepared catalytic materials' surface area and pore volumes were estimated using the BET method *via* the N_2-adsorption technique. Table 4 lists the surface area of the materials calculated *via* the N_2 adsorption–desorption technique. Compared to the other photocatalysts, the CZS-25 composite has the greatest surface area and a large pore volume. The Cu dopant inserted between the ZnO and SGN sheets might be responsible for the observed largest surface area of the CZS-25. Greater surface areas are thought to provide more active sites, allowing photocatalysts to absorb a greater number of contaminants on the surface. As a result, the CZS-25 may be likely to absorb and decompose the greatest amount of contaminants compared to other samples.[50,51]

3.7 Photoactivity

Fig. 8a and b shows the photocatalytic activity of ZnO and Cu-doped ZnO NPs (1–5%) against MB under sunlight. The sample-dye solutions were kept under dark for 1 hour before the photocatalysis to attain an adsorption–desorption equilibrium. The photocatalytic degradation rate of the MB dye and absorption graph of samples is shown in Fig. 8b. Maximal adsorption was achieved by 4-CZN NPs (16.7%), as compared to other samples (Fig. 8b).

The photocatalytic degradation of the MB solution was initiated by irradiating the sample-dye solutions, and Fig. 8a depicts the corresponding dye degradation behaviour of the photocatalysts. From the spectral graph, there is a gradual decline in dye degradation with time for all of the samples. 4-CZN NPs exhibit the maximum photocatalytic degradation of MB (82%) after 105 minutes (Fig. 8b), and this better photocatalytic activity of 4-CZN might happen due to the formation of additional trapping sites in 4-CZN due to optimum Cu doping into ZnO. These trapping sites (defects) minimize the e–h pair recombination by improving the induced charge carriers' lifetime and improving the dye degradation rate.[52]

As the photocatalytic efficiency of 4-CZN NPs against MB is not ideal, these NPs were coupled with variable concentrations of SGN to form nanocomposites (4% Cu–ZnO/SGN) with better photocatalytic efficiency. The detailed composition of the resultant NCs and their abbreviations are given in Table 2.

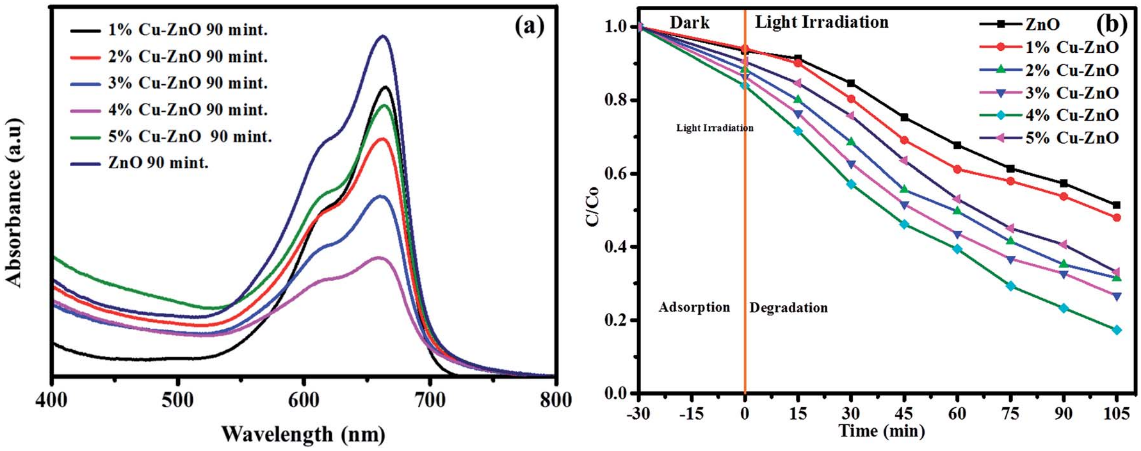

Fig. 8 Photocatalytic efficiency (a) and % degradation of MB (b) by ZnO and (1, 2, 3, 4, and 5 wt%) Cu–ZnO nanoparticles.

Fig. 9a reveals the photocatalytic activity of synthesized materials (SGN, 4-CZN, ZS, CZS-25, CZS-50, and CZS-75) against MB under sunlight. Before sunlight exposure, an adsorption–desorption equilibrium was achieved to explore the adsorption aptitudes of the samples by keeping each under dark for 60 minutes. Variable concentrations of MB were adsorbed by the fabricated materials, as given in Fig. 9a. The CZS-25 NC exhibited the maximum adsorption, as compared to other samples, because of its higher surface area and maximum pore size (Table 4).[53]

Remarkably, the 4% Cu–ZnO/S-g-C_3N_4 sample revealed an improved photocatalytic degradation of MB compared to the

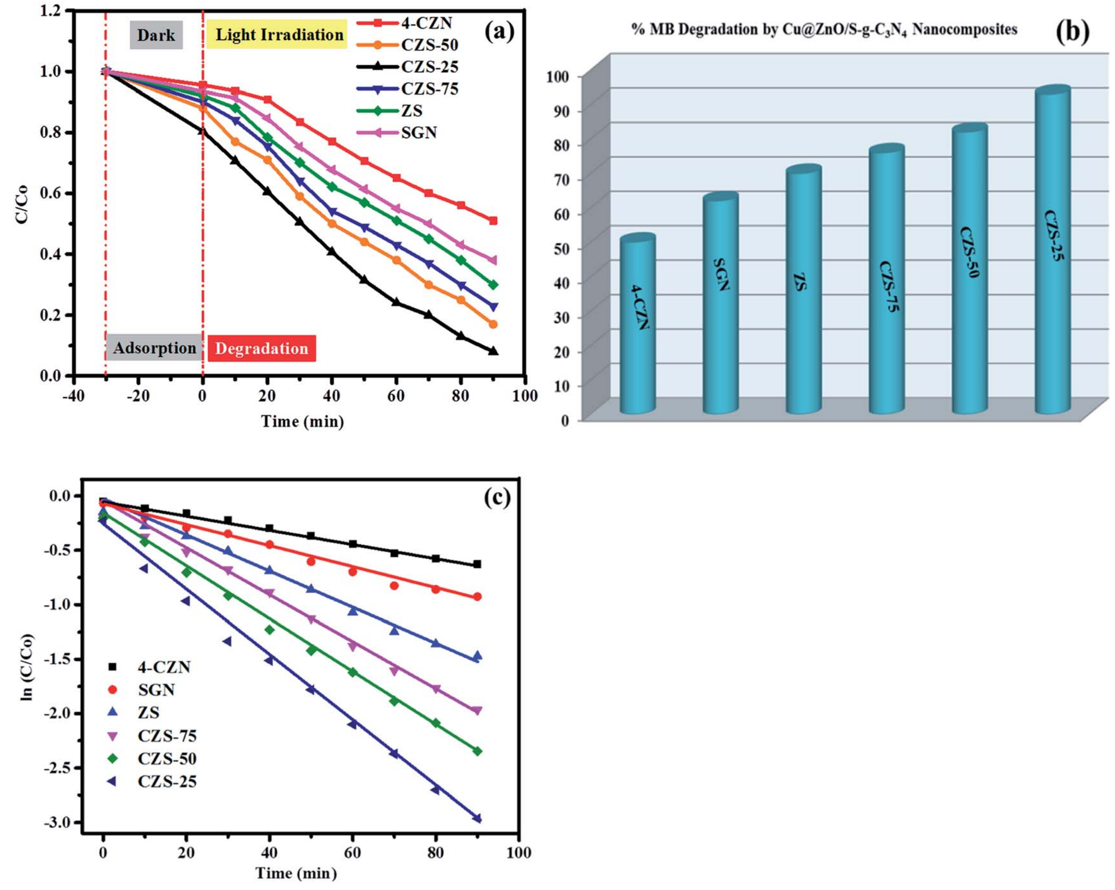

Fig. 9 Degradation rate (a), % degradation (b), and kinetic characteristics of MB under sunlight (c) by 4-CZN, ZS, SGN, CZS-25, CZS-50 and CZS-75 composites.

Table 5 Photocatalytic efficiency of 4% Cu–ZnO/S-g-C_3N_4 and some previous photocatalysts

S. no.	Composite	Organic pollutant	Light source	Irradiation time (min)	Percent degradation	Ref.
1	Cu doped ZnO/Cu/g-C_3N_4	MB	Visible	60	98	64
2	Mn–ZnO/RGO	RhB	Visible	140	99	65
3	Ag-doped g-C_3N_4	MB	Xe lamp	120	96	66
4	ZnO/Fe_3O_4/g-C_3N_4	MO	Visible	150	97.87	67
5	Cu–TiO_2	MB	Xe lamp	120	99	68
6	g-C_3N_4@Ag_2ZrO_3	RhB	Visible	120	99.70	69
7	Mn–ZnO/CSAC	BG	Solar	120	97.47	70
8	CZS-25	MB	Solar	90	93	Current study

SGN, 4-CZN, and ZS samples. The dye degradation rate for CZS-25 NC approaches 78% as compared to CZS-50 NC (62%) and CZS-75 NC (58%) after 60 minutes of sunlight illumination (Fig. 9a). Furthermore, the dye degradation rate of CZS-25 NC reached up to 93% after 90 minutes, as given by the bar graph in Fig. 9c. The enhanced dye degradation by the CZS-25 NC might be ascribed to the better charge separation. The fast charge transfer and enriched visible light absorption by CZS-25 NC are ascribed to the coupling of Cu–ZnO with SGN.[46,47] The electronic and optical properties of ZnO and SGN are significantly improved by Cu ion doping.[54,55] It might be the reason for the maximum photocatalytic efficiency of CZS-25 NC compared to the other synthesized composites.

From Fig. 9c, it is evident that the kinetics of the photocatalytic degradation of MB by NCs is pseudo-first-order. The value of k was calculated from the plot $\ln(C/C_o)$ *vs.* time t, as shown in Fig. 9c. The largest rate constant, 0.0334 min^{-1}, is found for CZS-25 NC because it decolorized the MB in 90 minutes. The "k" value of the ternary CZS-25 NC for MB degradation is almost 3 times greater than the "k" value of SGN (0.011 min^{-1}) and 5.5 times more than that of 4-CZN (0.006 min^{-1}). The order of the k values for the fabricated materials is as follows: CZS-25 NC (0.0334 min^{-1}) > CZS-50 NC (0.0210 min^{-1}) > CZS-75 NC (0.0171 min^{-1}) > ZS NC (0.0134 min^{-1}) > SGN (0.011 min^{-1}) > 4-CZN (0.006 min^{-1}). The maximum rate constant value observed for CZS-25 NC indicated that the synergistic effect between SGN, Cu, and ZnO has improved the number of active sites, and correspondingly enhanced the photocatalytic efficiency against MB dye.[56–58] Nonetheless, as the quantity of S-g-C_3N_4 in CZS NCs was increased beyond 25%, the photocatalytic performance of CZS NCs consistently decreased. This effect is consistent with previous findings, which show that as the constituent content surpasses the optimum value, the photocatalytic efficacy of the type-II nanoheterostructures decreases.[59–62]

The previous literature revealed that the photocatalytic efficiency of Cu-doped g-C_3N_4 and Cu-doped ZnO had been enhanced due to their improved charge carrier transportation, reduced particle size, and modified energy structure.[58,63] In addition, the photocatalytic efficiency of the CZS-25 NC is practically higher compared to the previously reported studies, as presented in Table 5.[64–70] Hence, the CZS-25 NC is the most effective composite for the photocatalytic dye degradation and was further employed for the recycling study.

3.8 Reusability and stability of the CZS-25 composite

As the durability of the photocatalyst under repetitive photocatalytic processes is essential for practical applications, the stability of the CZS-25 NCs was thus studied by MB dye degradation experiment up to six runs. As given in Fig. 10a, the CZS-25 NCs kept up the dye degradation rate, and no marked decline in catalytic efficiency was seen even after the twelfth consecutive cycle. Additionally, no marked change in XRD results of the CZS-25 NCs was detected after the twelfth cycle (Fig. 10b). Hence, the CZS-25 photocatalyst can be taken as a stable photocatalyst to be applied under sunlight.

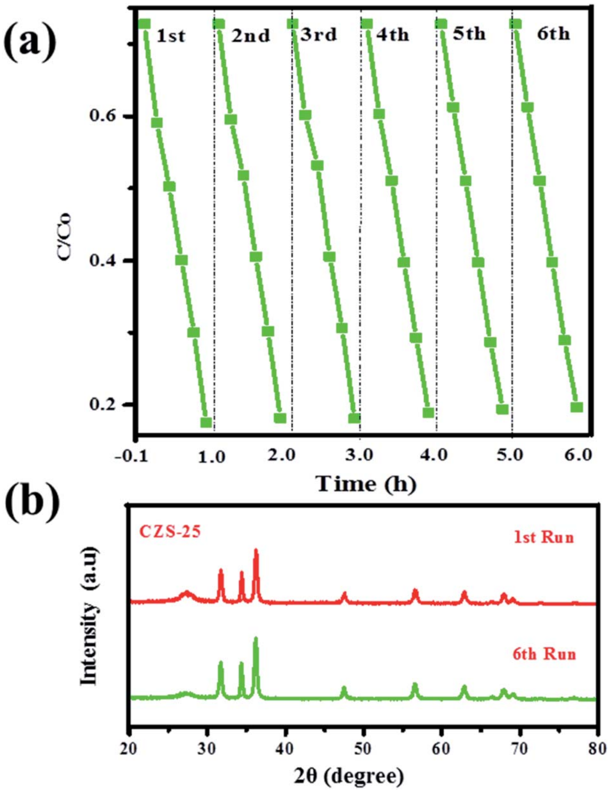

Fig. 10 The stability (a) XRD analysis (b) of CZS-25 after the 6th cycle.

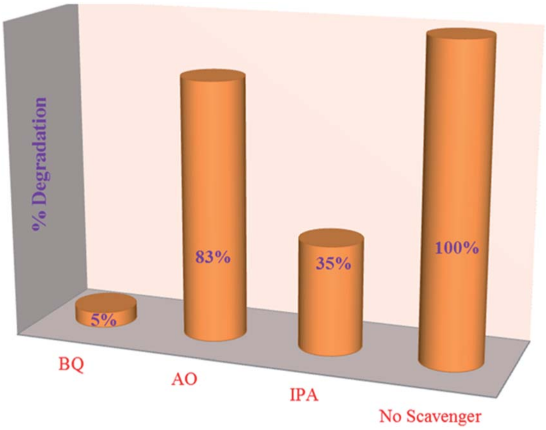

Fig. 11 Effect of scavengers on the photocatalytic degradation of MB by the 4% Cu–ZnO/S-g-C_3N_4 composite.

Table 6 Dye degradation inhibition of 4% Cu–ZnO/S-g-C_3N_4 by employed scavengers

Trapping agents	Captured species	% inhibition
Ammonium oxalate	h^+	17
Benzoquinone	$^{\bullet}O_2^{-}$	95
Isopropanol	$^{\bullet}OH$	65
No trapping agent	No capturing	00

3.9 Radical trapping experiments

To investigate the feasible dye degradation mechanism by the CZS-25 NC, it is critical to recognize the leading ROS for the photocatalytic degradation of MB. The photogenerated ROS produced during the dye degradation was captured by applying the important scavengers. The observed scavenger effect on the photocatalytic degradation of MB has been tabularized in Table 6 and given by Fig. 11.

These observations validate that the primary species involved in the photocatalytic degradation of MB are $^{\bullet}O^{2-}$ and $^{\bullet}OH$. Simultaneously, the holes with a 17% inhibition effect are the least effective active species for catalytic dye degradation.

3.10 Mechanism

The proposed photocatalytic MB degradation mechanism over the CZS-25 photocatalyst under sunlight radiation is depicted in Fig. 12. When CZS-25 NC is irradiated, e–h pairs are produced by sulphurized g-C_3N_4 and Cu-doped ZnO. The electrons from the valence band (VB) of ZnO and SGN are excited to the corresponding conduction band (CB). Then, these electrons from the CB of SGN are shifted to the CB of ZnO, owing to the lower CB edge potential (−0.5 eV) of ZnO than CB potential (−1.12 eV) of g-C_3N_4.[71–74] The doped Cu atoms in the CZS-25 NC at the SGN and ZnO interfaces function as mediators to transfer electrons from SGN to ZnO, and decrease the recombination frequency of electrons and holes. The electrons at the CB of ZnO are consumed in the induction of superoxide radicals (O_2^{-}) by reacting with chemisorbed O_2 on the surface of CZS-25 NC. Meanwhile, the h^+ in the VB of ZnO are migrated to the VB of g-C_3N_4 due to the lower VB potential of ZnO than the VB potential of g-C_3N_4.[75,76] The trapped holes on g-C_3N_4 yield hydroxyl radicals ($OH^{\bullet}$) by reacting with H_2O.[76,77] In addition, the accumulated h^+ in the VB of g-C_3N_4 might directly degrade MB.[78–82] The produced (O_2^{-} and $OH^{\bullet}$) reactive species interact with the MB molecules and decompose them by following a sequence of redox reactions, as given by eqn (2)–(6). The better photocatalytic activity of the CZS-25 NC might be ascribed to the suppressed e–h pairs recombination rate because of the

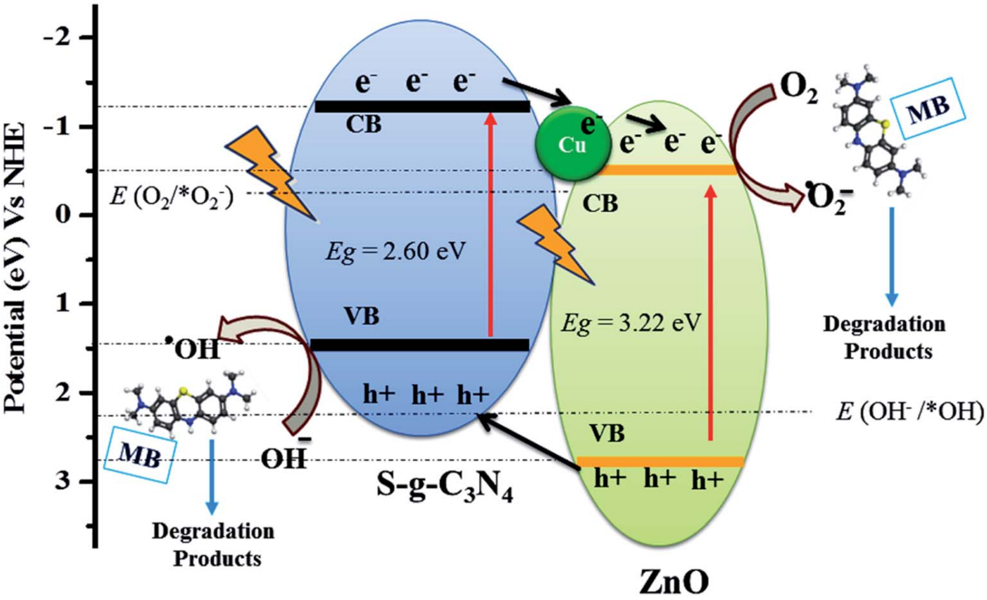

Fig. 12 A schematic MB photocatalytic degradation mechanism over the Cu@ZnO/S-g-C_3N_4 composite under sunlight.

synergetic effect between g-C_3N_4 and Cu-doped ZnO, and due to the formation of sufficient interfaces between these two phases.

$$\text{S-g-}C_3N_4\text{/Cu-doped ZnO} + h\upsilon \rightarrow \text{g-}C_3N_4\text{/Cu-doped ZnO } (e^-/h^+) \quad (2)$$

$$\text{Cu-doped ZnO } (e^-) + O_2 \rightarrow {}^{\bullet}O_2^- \quad (3)$$

$$\text{S-g-}C_3N_4 + H_2O/OH^- \rightarrow {}^{\bullet}OH \quad (4)$$

$$^{\bullet}OH/{}^{\bullet}O_2^- + \text{MB} \rightarrow \text{degraded products} \quad (5)$$

$$h^+ + \text{MB} \rightarrow \text{degraded products} \quad (6)$$

4. Conclusions

In conclusion, we successfully synthesized highly efficient Cu@ZnO/S-g-C_3N_4 photocatalysts *via* the chemical co-precipitation method. The characterization of the photocatalysts was done by TEM, XRD, EDX, FTIR, SEM and UV-visible, and PL spectroscopy. The comparative photocatalytic MB degradation revealed the excellent photocatalytic efficiency of CZS-25 NC compared to SGN, 4-CZN, ZS, CZS-50, and CZS-75 samples, and it degraded 100% of MB in 60 minutes under sunlight illumination. The well-developed interfaces between Cu–ZnO NPs and delicate sheets of SGN in the CZS-25 NC as depicted by morphological characterization favoured the effective charge conduction and harvesting of visible radiations. The improved photocatalytic activity of CZS-25 NC might be attributed to effective e–h pair separation due to the establishment of a well-defined heterojunction among the ZnO, SGN, and Cu ions. Overall, the present research outcomes provide us with new insight into the synthesis of photocatalytic materials and their applications for organic pollution degradation from wastewater.

Conflicts of interest

The authors hereby declare that there is no conflict of interest and satisfy all ethics in publishing policy.

Acknowledgements

The authors gratefully acknowledge the support received for this research work from the HEC start up grant (SRGP Project No. 2272) and Department of Chemistry, University of Management & Technology, Lahore-54770, Pakistan.

References

1 X. F. Liang, G. L. Wang, X. L. Dong, G. W. Wang, H. C. Ma and X. F. Zhang, Graphitic carbon nitride with carbon vacancies for photocatalytic degradation of bisphenol A, *ACS Appl. Nano Mater.*, 2019, **2**, 517–524.

2 X. B. Feng, H. M. Ju, T. H. Song, T. S. Fang, W. C. Liu and W. Huang, Highly efficient photocatalytic degradation performance of $CsPb(Br_{1-x}Cl_x)_3$-Au nanoheterostructures, *ACS Sustainable Chem. Eng.*, 2019, **7**, 5152–5156.

3 R. C. Ding, Y. Z. Fan and G. S. Wang, High efficient Cu_2O/TiO_2 nanocomposite Photocatalyst todegrade organic Polluant under visible light irradiation, *ChemistrySelect*, 2018, **3**, 1682–1687.

4 J. N. Schrauben, R. Hayoun, C. N. Valdez, M. Braten, L. Fridley and J. M. Mayer, Titanium and zinc oxide nanoparticles are proton-coupled electron transfer agents, *Science*, 2012, **336**, 1298–1301.

5 D. Vidyasagar, S. G. Ghugal, A. Kulkarni, A. G. Shende, S. S. Umare and R. Sasikala, Microwave assisted: *in situ* decoration of a g-C_3N_4 surface with $CdCO_3$ nanoparticles for visible light driven photocatalysis, *New J. Chem.*, 2018, **42**, 6322–6331.

6 G. Mamba and A. K. Mishra, Graphitic carbon nitride (g-C_3N_4) nanocomposites: a new and exciting generation of visible light driven photocatalysts for environmental pollution remediation, *Appl. Catal., B*, 2016, **198**, 347–377.

7 K. Ravichandran and E. Sindhuja, Fabrication of cost effective g-C_3N_4+Ag activated ZnO photocatalyst in thin film form for enhanced visible light responsive dye degradation, *Mater. Chem. Phys.*, 2019, **221**, 203–215.

8 J. Šíma and P. Hasal, Photocatalytic degradation of textile dyes in a TiO_2/UV system, *Chem. Eng. J.*, 2013, **32**, 79–84.

9 M. Mousavi, A. Habibi-Yangjeh and S. R. Pouran, Review on the criteria anticipated for the fabrication of highly efficient ZnO-based visible-light-driven photocatalysts, *J. Ind. Eng. Chem.*, 2018, **62**, 1–25.

10 S. Iqbal, Spatial charge separation and transfer in L-cysteine capped NiCoP/CdS nano-heterojunction activated with intimate covalent bonding for high-quantum-yield photocatalytic hydrogen evolution, *Appl. Catal.*, 2020, **274**, 119097.

11 K. S. Siddiqi, A. Ur Rahman and A. T. Husen, Properties of zinc oxide nanoparticles and their activity against microbes, *Nanoscale Res. Lett.*, 2018, **13**, 141.

12 M. Shekofteh-Gohari, A. Habibi-Yangjeh, M. Abitorabi and A. Rouhi, Magnetically separable nanocomposites based on ZnO and their applications in photocatalytic processes: a review, *Crit. Rev. Environ. Sci. Technol.*, 2018, **48**, 806–857.

13 S. Liang, K. Xiao, Y. Mo and X. Huang, A novel ZnO nanoparticle blended poly-vinylidene fluoride membrane for anti-irreversible fouling, *J. Membr. Sci.*, 2012, **394**, 184–192.

14 I. Djerdj, Z. Jagličić, D. Arčon and M. Niederberger, Co-doped ZnO nanoparticles: minireview, *Nanoscale*, 2010, **2**, 1096–1104.

15 O. Długosz, K. Szostak and M. Banach, Photocatalytic properties of zirconium oxide-zinc oxide nanoparticles synthesised using microwave irradiation, *Appl. Nanosci.*, 2020, **10**, 941–954.

16 A. M. Tama, S. Das, S. Dutta, M. D. I. Bhuyan, M. N. Islam and M. A. Basith, MoS_2 nanosheet incorporated α-Fe_2O_3/ZnO nanocomposite with enhanced photocatalytic dye degradation and hydrogen production ability, *RSC Adv.*, 2019, **9**, 40357–40367.

17 S. Iqbal, M. Javed, A. Bahadur, M. A. Qamar, M. Ahmad, M. Shoaib, M. Raheel, N. Ahmad, M. B. Akbar and H. Li, Controlled synthesis of Ag-doped CuO nanoparticles as a core with poly(acrylic acid) microgel shell for efficient removal of methylene blue under visible light, *J. Mater. Sci.: Mater. Electron.*, 2020, **31**, 8423–8435.

18 V. Vaiano, G. Iervolino and L. Rizzo, Cu-doped ZnO as efficient photocatalyst for the oxidation of arsenite to arsenate under visible light, *Appl. Catal., B*, 2018, **238**, 471–479.

19 T. Welderfael, O. P. Yadav, A. M. Taddesse and J. Kaushal, Synthesis, characterization and photocatalytic activities of Ag-N-codoped ZnO nanoparticles for degradation of methyl red, *Bull. Chem. Soc. Ethiop.*, 2013, **27**, 221–232.

20 Y. Lv, J. Lin, S. Peng, L. Zhang and L. Yu, Effective ways to enhance the photocatalytic activity of ZnO nanopowders: high crystalline degree, more oxygen vacancies, and preferential growth, *New J. Chem.*, 2019, **43**, 19223–19231.

21 S. Kuriakose, B. Satpati and S. Mohapatra, Highly efficient photocatalytic degradation of organic dyes by Cu doped ZnO nanostructures, *Phys. Chem. Chem. Phys.*, 2015, **17**, 25172–25181.

22 A. N. Kadam, T. G. Kim, D. S. Shin, K. M. Garadkar and J. Park, Morphological evolution of Cu doped ZnO for enhancement of photocatalytic activity, *J. Alloys Compd.*, 2017, **710**, 102–113.

23 V. Vaiano, G. Iervolino and L. Rizzo, Cu-doped ZnO as efficient photocatalyst for the oxidation of arsenite to arsenate under visible light, *Appl. Catal., B*, 2018, **238**, 471–479.

24 M. R. D. Khaki, M. S. Shafeeyan, A. A. A. Raman and W. M. A. W. Daud, Enhanced UV–Visible photocatalytic activity of Cu-doped ZnO/TiO_2 nanoparticles, *J. Mater. Sci.: Mater. Electron.*, 2018, **29**, 5480–5495.

25 M. Samadi, H. A. Shivaee, A. Pourjavadi and A. Z. Moshfegh, Synergism of oxygen vacancy and carbonaceous species on enhanced photocatalytic activity of electrospun ZnO-carbon nanofibers: charge carrier scavengers mechanism, *Appl. Catal., A*, 2013, **466**, 153–160.

26 S. Zhang, C. Su, H. Ren, M. Li, L. Zhu, S. Ge, M. Wang, Z. Zhang, L. Li and X. Cao, In situ fabrication of ZnO/g-C3N4 nanocomposites for photocatalytic degradation of methylene blue: synthesis procedure does matter, *Nanomaterials*, 2019, **9**, 215.

27 R. Kuriki, K. Sekizawa, O. Ishitani and K. Maeda, Visible-light-driven CO 2 reduction with carbon nitride: enhancing the activity of ruthenium catalysts, *Angew. Chem., Int. Ed.*, 2015, **54**, 2406–2409.

28 J. Wang, Z. Yang, X. Gao, W. Yao, W. Wei, X. Chen and Y. Zhu, Core-shell g-C_3N_4@ZnO composites as photoanodes with double synergistic effects for enhanced visible-light photoelectrocatalytic activities, *Appl. Catal., B*, 2017, **217**, 169–180.

29 J. Hong, X. Xia, Y. Wang and R. Xu, Mesoporous carbon nitride with *in situ* sulfur doping for enhanced photocatalytic hydrogen evolution from water under visible light, *J. Mater. Chem.*, 2012, **22**, 15006–15012.

30 K. Wang, Q. Li, B. Liu, B. Cheng, W. Ho and J. Yu, Sulfur-doped g-C3N4 with enhanced photocatalytic CO2-reduction performance, *Appl. Catal., B*, 2015, **176–177**, 44–52.

31 Q. Fan, J. Liu, Y. Yu, S. Zuo and B. Li, A simple fabrication for sulfur doped graphitic carbon nitride porous rods with excellent photocatalytic activity degrading RhB dye, *Appl. Surf. Sci.*, 2017, **391**, 360–368.

32 L. Jiang, X. Yuan, Y. Pan, J. Liang, G. Zeng, Z. Wu and H. Wang, Doping of graphitic carbon nitride for photocatalysis: a review, *Appl. Catal., B*, 2017, **217**, 388–406.

33 M. Sher, M. Javed, S. Shahid, S. Iqbal, M. A. Qamar, A. Bahadur and M. A. Qayyum, The controlled synthesis of g-C_3N_4/Cd-doped ZnO nanocomposites as potential photocatalysts for the disinfection and degradation of organic pollutants under visible light irradiation, *RSC Adv.*, 2020, **11**, 2025–2039.

34 K. Wang, Q. Li, B. Liu, B. Cheng, W. Ho and J. Yu, Sulfur-doped g-C_3N_4 with enhanced photocatalytic CO_2-reduction performance, *Appl. Catal., B*, 2015, **176–177**, 44–52.

35 X. Yang, Z. Tian, Y. Chen, H. Huang, J. Hu and B. Wen, In situ synthesis of 2D ultrathin cobalt doped g-C_3N_4 nanosheets enhances photocatalytic performance by accelerating charge transfer, *J. Alloys Compd.*, 2021, **859**, 157754.

36 X. Wu, Z. Wei, L. Zhang, X. Wang, H. Yang and J. Jiang, Optical and magnetic properties of Fe doped ZnO nanoparticles obtained by hydrothermal synthesis, *J. Nanomater.*, 2014, **2014**, 4.

37 Y. P. Zhu, M. Li, Y. L. Liu, T. Z. Ren and Z. Y. Yuan, Carbon-doped ZnO hybridized homogeneously with graphitic carbon nitride nanocomposites for photocatalysis, *J. Phys. Chem. C*, 2014, **118**, 10963–10971.

38 M. F. Manzoor, E. Ahmad, M. Ullah, A. M. Rana, A. S. Malik, M. Farooq, I. Ahmad, M. Hasnain, Z. A. Shah, W. Q. Khan and U. Mehtab, Impact of Copper Doping on the Structural, Electrical and Optical Properties of Auto-Combustion Synthesized ZnO Nanocomposites, *Acta Phys. Pol., A*, 2019, **135**, 458–466.

39 Y. H. Lu, W. H. Lin, C. Y. Yang, Y. H. Chiu, Y. C. Pu, M. H. Lee, Y. C. Tseng and Y. J. Hsu, A facile green antisolvent approach to Cu^{2+}-doped ZnO nanocrystals with visible-light-responsive photoactivities, *Nanoscale*, 2014, **6**, 8796–8803.

40 S. C. Yan, Z. S. Li and Z. G. Zou, Photodegradation performance of g-C_3N_4 fabricated by directly heating melamine, *Langmuir*, 2009, **25**, 10397–10401.

41 F. Guo, W. Shi, W. Guan, H. Huang and Y. Liu, Carbon dots/g-C_3N_4/ZnO nanocomposite as efficient visible-light driven photocatalyst for tetracycline total degradation, *Sep. Purif. Technol.*, 2017, **173**, 295–303.

42 S. P. Adhikari, H. R. Pant, H. J. Kim, C. H. Park and C. S. Kim, One pot synthesis and characterization of Ag-ZnO/g-C_3N_4 photocatalyst with improved photoactivity and antibacterial properties, *Colloids Surf., A*, 2015, **482**, 477–484.

43 G. Di, Z. Zhu, H. Zhang, J. Zhu, Y. Qiu, D. Yin and S. Küppers, Visible-light degradation of sulfonamides by Z-scheme ZnO/

$g\text{-}C_3N_4$ heterojunctions with amorphous Fe_2O_3 as electron mediator, *J. Colloid Interface Sci.*, 2019, **538**, 256–266.

44 N. Kumaresan, M. M. A. Sinthiya, M. Sarathbavan, K. Ramamurthi, K. Sethuraman and R. R. Babu, Synergetic effect of $g\text{-}C_3N_4$/ZnO binary nanocomposites heterojunction on improving charge carrier separation through 2D/1D nanostructures for effective photocatalytic activity under the sunlight irradiation, *Sep. Purif. Technol.*, 2019, 116356.

45 D. Jiang, L. Chen, J. Xie and M. Chen, Ag_2S/$g\text{-}C_3N_4$ composite photocatalysts for efficient Pt-free hydrogen production. The co-catalyst functions of Ag/Ag_2S formed by simultaneous photodeposition, *Dalton Trans.*, 2014, **43**, 4878–4885.

46 N. Kumaresan, M. M. Sinthiya, M. P. Kumar, S. Ravichandran, R. R. Babu, K. Sethurman and K. Ramamurthi, Investigation on the $g\text{-}C_3N_4$ encapsulated ZnO nanorods heterojunction coupled with GO for effective photocatalytic activity under visible light irradiation, *Arabian J. Chem.*, 2020, **13**, 2826–2843.

47 L. N. Tong, T. Cheng, H. B. Han, J. L. Hu, X. M. He, Y. Tong and C. M. Schneider, Photoluminescence studies on structural defects and room temperature ferromagnetism in Ni and Ni–H doped ZnO nanoparticles, *J. Appl. Phys.*, 2010, **108**, 023906.

48 D. Theyvaraju and S. Muthukumaran, Microstructure, crystallographic and photoluminescence examination of Ni doped ZnO nanoparticles Co-doped with Co by sol–gel method, *J. Inorg. Organomet. Polym. Mater.*, 2017, **27**, 1572–1582.

49 Y. A. Chen, Y. T. Wang, H. S. Moon, K. Yong and Y. J. Hsu, Yolk-shell nanostructures: synthesis, photocatalysis and interfacial charge dynamics, *RSC Adv.*, 2021, **20**, 12288–12305.

50 A. J. Reddy, M. K. Kokila, H. Nagabhushana, R. P. S. Chakradhar, C. Shivakumara, J. L. Rao and B. M. Nagabhushana, *J. Alloys Compd.*, 2011, **509**, 5349–5355.

51 M. A. Mohamed, M. F. M. Zain, L. J. Minggu, M. B. Kassim, J. Jaafar, N. A. S. Amin, M. S. Mastuli, H. Wu, R. J. Wong and Y. H. Ng, Bio-inspired hierarchical hetero-architectures of in situ C-doped $g\text{-}C_3N_4$ grafted on C, N co-doped ZnO micro-flowers with booming solar photocatalytic activity, *J. Ind. Eng. Chem.*, 2019, **77**(25), 393–407.

52 D. Neena, M. Humayun, D. Bhattacharyya and D. Fu, Hierarchical Sr-ZnO/$g\text{-}C_3N_4$ heterojunction with enhanced photocatalytic activities, *J. Photochem. Photobiol., A*, 2020, 112515.

53 Y. Matsukawa, S. Hirata, M. Inada, N. Enomoto, J. Hojo and K. Hayashi, Kinetic effects of polymorphs and surface areas on adsorption and photocatalytic decomposition of acetaldehyde on titania, *Chem. Eng. J.*, 2020, 125422.

54 R. S. Das, S. K. Warkhade, A. Kumar, G. S. Gaikwad and A. V. Wankhade, Graphitic carbon nitride@silver zirconate nanocomposite ($g\text{-}C_3N_4$@Ag_2ZrO_3): a type-II heterojunction for an effective visible light photocatalysis and bacterial photo-inactivation, *J. Alloys Compd.*, 2020, 155770.

55 M. Rashid, M. Ikram, A. Haider, S. Naz, J. Haider, A. Ul-Hamid, A. Shahzadi and M. Aqeel, Photocatalytic, dye degradation, and bactericidal behavior of Cu-doped ZnO nanorods and their molecular docking analysis, *Dalton Trans.*, 2020, **49**, 8314–8330.

56 D. Toloman, A. Popa, M. Stan, M. Stefan, G. Vlad, S. Ulinici, G. Baisan, T. D. Silipas, S. Macavei, C. Leostean and S. Pruneanu, Visible-light-driven photocatalytic degradation of different organic pollutants using Cu doped ZnO-MWCNT nanocomposites, *J. Alloys Compd.*, 2021, **866**, 159010.

57 D. D. Qin, J. J. Quan, S. F. Duan, J. San Martin, Y. Lin, X. Zhu, X. Q. Yao, J. Z. Su, I. Rodríguez-Gutiérrez, C. L. Tao and Y. Yan, High-performance photoelectrochemical water oxidation with phosphorus-doped and metal phosphide co catalyst-modified $g\text{-}C_3N_4$ formation through gas treatment, *ChemSusChem*, 2019, **12**, 898–907.

58 F. Guo, W. Shi, W. Guan, H. Huang and Y. Liu, Carbon dots/$g\text{-}C_3N_4$/ZnO nanocomposite as efficient visible-light driven photocatalyst for tetracycline total degradation, *Sep. Purif. Technol.*, 2017, **173**, 295–303.

59 Y. F. Lin and Y. J. Hsu, Interfacial charge carrier dynamics of type-II semiconductor nanoheterostructures, *Appl. Catal., B*, 2013, **130**, 93–98.

60 T. H. Lai, K. I. Katsumata and Y. J. Hsu, In situ charge carrier dynamics of semiconductor nanostructures for advanced photoelectrochemical and photocatalytic applications, *Nanophotonics*, 2021, **10**, 777–795.

61 C. W. Tsao, M. J. Fang and Y. J. Hsu, Modulation of interfacial charge dynamics of semiconductor heterostructures for advanced photocatalytic applications, *Coord. Chem. Rev.*, 2021, **438**, 213876.

62 Y. H. Chiu, T. F. M. Chang, C. Y. Chen, M. Sone and Y. J. Hsu, Mechanistic insights into photodegradation of organic dyes using heterostructure photocatalysts, *Catalysts*, 2019, **9**, 430.

63 D. Toloman, A. Popa, M. Stan, M. Stefan, G. Vlad, S. Ulinici, G. Baisan, T. D. Silipas, S. Macavei, C. Leostean and S. Pruneanu, Visible-light-driven photocatalytic degradation of different organic pollutants using Cu doped ZnO-MWCNT nanocomposites, *J. Alloys Compd.*, 2021, **866**, 159010.

64 M. A. Bajiri, A. Hezam, N. Keerthiraj, B. M. Al-Maswari, H. S. B. Naik, K. Byrappa and R. AlasmariNon-Noble, Metallic Cu with Three Different Roles in Cu doped ZnO/Cu/$g\text{-}C_3N_4$ Heterostructure for Enhanced Z-Scheme Photocatalytic Activity, *New J. Chem.*, 2021, **45**, 13499–13511.

65 P. K. Labhane, L. B. Patle, G. H. Sonawane and S. H. Sonawane, Fabrication of ternary Mn doped ZnO nanoparticles grafted on reduced graphene oxide (RGO) sheet as an efficient solar light driven photocatalyst, *Chem. Phys. Lett.*, 2018, **710**, 70–77.

66 D. R. Paul, R. Sharma, P. Panchal, R. Malik, A. Sharma, V. K. Tomer and S. P. Nehra, Silver doped graphitic carbon nitride for the enhanced photocatalytic activity towards organic dyes, *J. Nanosci.*, 2019, **19**, 5241–5248.

67 Z. Wu, X. Chen, X. Liu, X. Yang and Y. Yang, A ternary magnetic recyclable ZnO/Fe_3O_4/$g\text{-}C_3N_4$ composite photocatalyst for efficient photodegradation of monoazo dye, *Nanoscale Res. Lett.*, 2019, **14**, 147–151.

68 L. Anju Chanu, W. Joychandra Singh, K. Jugeshwar Singh and K. Nomita Devi, Effect of operational parameters on the photocatalytic degradation of Methylene blue dye solution using manganese doped ZnO nanoparticles, *Results Phys.*, 2019, **12**, 1230–1237.

69 M. Ikram, E. Umar, A. Raza, A. Haider, S. Naz, D. A. Ul-Hamid, J. Haider, I. Shahzadi, J. Hassan and S. Ali, Dye degradation performance, bactericidal behavior and molecular docking analysis of Cu-doped TiO_2 nanoparticles, *RSC Adv.*, 2020, **10**, 24215–24233.

70 R. S. Das, S. K. Warkhade, A. Kumar, G. S. Gaikwad and A. V. Wankhade, Graphitic carbon nitride@silver zirconate nanocomposite ($g-C_3N_4@Ag_2ZrO_3$): a type-II heterojunction for an effective visible light photocatalysis and bacterial photo inactivation, *J. Alloys Compd.*, 2020, 155770.

71 R. Nithya, S. Ragupathy, D. Sakthi, V. Arun and N. Kannadasan, A study on Mn doped ZnO loaded on CSAC for the photocatalytic degradation of brilliant green dye, *Chem. Phys. Lett.*, 2020, **755**, 137769.

72 S. Ma, S. Zhan, Y. Xia, P. Wang, Q. Hou and Q. Zhou, Enhanced photocatalytic bactericidal performance and mechanism with novel $Ag/ZnO/g-C_3N_4$ composite under visible light, *Catal. Today*, 2019, **330**, 179–188.

73 Y. Wu, Y. Zhou, H. Xu, Q. Liu, Y. Li, L. Zhang, H. Liu, Z. Tu and X. Cheng, Highly active, superstable, and biocompatible $Ag/polydopamine/g-C_3N_4$ bactericidal photocatalyst: synthesis, characterization, and mechanism, *ACS Sustainable Chem. Eng.*, 2018, **6**, 14082–14094.

74 J. C. Wang, H. C. Yao, Z. Y. Fan, L. Zhang, J. S. Wang, S. Q. Zang and Z. J. Li, Indirect Z- scheme $BiOI/g-C_3N_4$ photocatalysts with enhanced photoreduction CO_2 activity under visible light irradiation, *ACS Appl. Mater. Interfaces*, 2016, **8**, 3765–3775.

75 S. C. Yan, S. B. Lv, Z. S. Li and Z. G. Zou, Organic-inorganic composite photocatalyst of $g-C_3N_4$ and TaON with improved visible light photocatalytic activities, *Dalton Trans.*, 2010, **39**, 1488–1491.

76 Y. Feng, Y. Wang, M. Li, S. Lv, W. Li and Z. Li, Novel visible light induced $Ag_2S/g-C_3N_4/ZnO$ nanoarrays heterojunction for efficient photocatalytic performance, *Appl. Surf. Sci.*, 2018, **462**, 896–903.

77 M. J. Fang, C. W. Tsao and Y. J. Hsu, Semiconductor nanoheterostructures for photoconversion applications, *J. Phys. D: Appl. Phys.*, 2020, **53**, 143001.

78 M. A. Qamar, S. Shahid and M. Javed, Synthesis of dynamic $g-C_3N_4/Fe@ZnO$ nanocomposites for environmental remediation applications, *Ceram. Int.*, 2020, **46**, 22171–22180.

79 M. A. Qamar, S. Shahid, S. A. Khan, S. Zaman and M. N. Sarwar, Synthesis characterization, optical and antibacterial studies of Co-doped SnO_2 nanoparticles, *Dig. J. Nanomater. Biostructures*, 2017, **12**, 1127–1135.

80 M. A. Qamar, S. Shahid, M. Javed, S. Iqbal, M. Sher and M. B. Akbar, Highly efficient $g-C_3N_4/Cr-ZnO$ nanocomposites with superior photocatalytic and antibacterial activity, *J. Photochem. Photobiol., A*, 2020, **401**, 112776.

81 S. Iqbal, N. Ahmad, M. A. Qamar, M. Javed, A. Bahadur, S. Ali, Z. Ahmad, R. M. Irfan, G. Liu, M. B. Akbar and M. A. Qayyum, Designing highly potential photocatalytic comprising silver deposited ZnO NPs with sulfurized graphitic carbon nitride ($Ag/ZnO/Sg-C_3N_4$) ternary composite, *J. Environ. Chem. Eng.*, 2020, **9**(2021), 104919.

82 M. A. Qamar, S. Shahid, M. Javed, M. Sher, S. Iqbal, A. Bahadur and D. Li, Fabricated novel $g-C_3N_4/Mn$ doped ZnO nanocomposite as highly active photocatalyst for the disinfection of pathogens and degradation of the organic pollutants from wastewater under sunlight radiations, *Colloids Surf., A*, 2020, 125863.